

Bifurcation dynamics govern sharp wave ripple generation and rhythmic transitions in hippocampal-cortical memory networks

Xin Jiang(姜鑫), Jialiang Nie(聂嘉良), Denggui Fan(樊登贵), and Lixia Duan(段利霞)
Citation: Chin. Phys. B, 2025, 34 (**12**): 128702. DOI: 10.1088/1674-1056/ae111d
http://cpb.iphy.ac.cn; http://iopscience.iop.org/cpb

What follows is a list of articles you may be interested in

Effects of information and policy regulation on green behavior propagation in multilayer networks: Modeling, analysis, and optimal allocation

Xian-Li Sun(孙先莉), and Ling-Hua Zhang(张玲华)
Chin. Phys. B, 2025, 34 (**6**): 068704. DOI: 10.1088/1674-1056/adbedf

Triadic percolation in computer virus spreading dynamics

Jie Gao(高杰), Jianfeng Luo(罗建锋), Xing Li(李星), Yihong Li(李毅红), Zunguang Guo(郭尊光), and Xiaofeng Luo(罗晓峰)
Chin. Phys. B, 2025, 34 (**2**): 028701. DOI: 10.1088/1674-1056/ad9ff8

Dual mechanisms of Bcl-2 regulation in IP_3-receptor-mediated Ca^{2+} release: A computational study

Hong Qi(祁宏), Zhi-Qiang Shi(史志强), Zhi-Chao Li(李智超), Chang-Jun Sun(孙长君), Shi-Miao Wang(王世苗), Xiang Li(李翔), and Jian-Wei Shuai(帅建伟)
Chin. Phys. B, 2021, 30 (**10**): 108704. DOI: 10.1088/1674-1056/ac1e0d

Dynamics and coherence resonance in a thermosensitive neuron driven by photocurrent

Ying Xu(徐莹), Minghua Liu(刘明华), Zhigang Zhu(朱志刚), Jun Ma(马军)
Chin. Phys. B, 2020, 29 (**9**): 098704. DOI: 10.1088/1674-1056/ab9dee

Generating mechanism of pathological beta oscillations in STN-GPe circuit model: A bifurcation study

Jing-Jing Wang(王静静), Yang Yao(姚洋), Zhi-Wei Gao(高志伟), Xiao-Li Li(李小俚), Jun-Song Wang(王俊松)
Chin. Phys. B, 2020, 29 (**5**): 058701. DOI: 10.1088/1674-1056/ab7e9b

---

SPECIAL TOPIC — Biophysical circuits: Modeling & applications in neuroscience

Bifurcation dynamics govern sharp wave ripple generation and rhythmic transitions in hippocampal-cortical memory networks

Xin Jiang(姜鑫)[1], Jialiang Nie(聂嘉良)[1], Denggui Fan(樊登贵)[2], and Lixia Duan(段利霞)[1,†]

[1] *College of Science, North China University of Technology, Beijing* 100144, *China*

[2] *School of Mathematics and Physics, University of Science and Technology Beijing, Beijing* 100083, *China*

(Received 25 August 2025; revised manuscript received 29 September 2025; accepted manuscript online 9 October 2025)

This study investigates the bifurcation dynamics underlying rhythmic transitions in a biophysical hippocampal–cortical neural network model. We specifically focus on the membrane potential dynamics of excitatory neurons in the hippocampal CA3 region and examine how strong coupling parameters modulate memory consolidation processes. Employing bifurcation analysis, we systematically characterize the model's complex dynamical behaviors. Subsequently, a characteristic waveform recognition algorithm enables precise feature extraction and automated detection of hippocampal sharp-wave ripples (SWRs). Our results demonstrate that neuronal rhythms exhibit a propensity for abrupt transitions near bifurcation points, facilitating the emergence of SWRs. Critically, temporal rhythmic analysis reveals that the occurrence of a bifurcation is not always sufficient for SWR formation. By integrating one-parameter bifurcation analysis with extremum analysis, we demonstrate that large-amplitude membrane potential oscillations near bifurcation points are highly conducive to SWR generation. This research elucidates the mechanistic link between changes in neuronal self-connection parameters and the evolution of rhythmic characteristics, providing deeper insights into the role of dynamical behavior in memory consolidation.

Keywords: hippocampal-cortical memory networks, bifurcation analysis, rhythmic transitions, sharp wave ripples

PACS: 87.23.Kg, 87.19.ll, 87.19.lv, 87.10.Ed

DOI: 10.1088/1674-1056/ae111d **CSTR:** 32038.14.CPB.ae111d

1. Introduction

Memory refers to the cognitive process through which the human brain encodes, stores, consolidates and retrieves information acquired from the external environment.[1,2] Memory consolidation constitutes a critical and indispensable component of the overall memory process. Experimental evidence demonstrates that the hippocampus, cerebral cortex and thalamus are recognized as key brain regions involved in memory consolidation.[3–5] When the brain acquires new information, the hippocampus is responsible for encoding short-term memory into long-term memory, a process that involves changes in synaptic plasticity among brain neurons.[6] During the memory encoding process in the hippocampus, the cerebral cortex actively participates in this stage, which supports the transformation of short-term memory representations into stable long-term memory traces.[7] The thalamus exhibits enhanced functional connectivity with motor-related cortical regions.[8]

In recent years, as research on the effects of brain neural activity during sleep on memory processes has progressed, three key types of neuronal activities — hippocampal sharp-wave ripples (SWRs), cortical slow oscillations (SOs) and thalamic spindles — have been identified through numerous physiological experiments, shedding light on their underlying functional mechanisms. Hippocampal SWRs are prominent, irregular and spontaneous transient electrical events that occur during the resting state. They consist of high-frequency ripple oscillations (110–250 Hz) superimposed on lower-frequency sharp waves (0.01–3 Hz), with each event typically lasting 50–100 ms.[9] They often occur during slow-wave sleep (SWS), acting as a core mechanism for memory replay and the transfer of information from the hippocampus to the neocortex.[11,12] The generation of hippocampal SWRs is critically dependent on the synchronous burst firing of pyramidal neurons in the CA3 subregion and the modulatory influence of local inhibitory interneurons in the CA1 subregion.[13] Research indicates that during sleep, hippocampal SWRs facilitate the consolidation of newly acquired memories through the reactivation of neural activity patterns experienced during wakefulness.[14] SWRs also contribute to path planning during spatial navigation[15] and the modulation of synaptic plasticity.[16] Experimental evidence suggests that excessively high SWR frequency can significantly impair the consolidation of spatial and episodic memory.[17,18] In severe cases, it may contribute to the development of neurological disorders such as temporal lobe epilepsy[19] and Alzheimer's disease.[20] The slow oscillations (< 1 Hz) of

†Corresponding author. E-mail: duanlx@ncut.edu.cn

© 2025 Chinese Physical Society and IOP Publishing Ltd. All rights, including for text and data mining, AI training, and similar technologies, are reserved.

the cerebral cortex represent the predominant rhythm during sleep, primarily characterized by alternating phases of neuronal activity between depolarization (up state) and hyperpolarization (down state).[21] During this process, cortical slow oscillations contribute significantly to memory consolidation through the coordination of neural activity.[22] Thalamic spindles (10–16 Hz) originate from the thalamocortical circuit and are predominantly observed during SWS, particularly during the second stage of non-rapid eye movement (N2) sleep.[23] Thalamic sleep spindles facilitate the consolidation of motor memory.[24] The generation of spindles is strongly associated with improved performance following memory-related learning tasks.[25] Recent studies have demonstrated that spindle oscillations frequently occur during the up-state phase of slow oscillations and participate in cross-regional coordinated dynamics in conjunction with SWRs. The temporal coordination among these characteristic waveforms across brain regions elucidates the neural dynamical mechanisms underlying sleep-dependent systematic memory consolidation.[26,27]

In recent years, researchers have developed numerous computational models for neural memory mechanisms and conducted extensive dynamical analyses. Ghorbani *et al.*[26] proposed a three-phase coupled unified network model incorporating both excitatory and inhibitory neurons in the cerebral cortex. Based on the average neuronal activity, researchers have qualitatively characterized features of up–down state oscillations in cortical neurons. Foroutannia *et al.*[28] investigated the Lyapunov exponent and bifurcation diagram of a cortical neuron model, revealing that synaptic connection strength has a significant impact on bifurcation dynamics. To validate the hypothesis that nonlinear interactions between cortical high-frequency oscillations and thalamic activities may give rise to slow spindles, Foroutannia *et al.* proposed a simplified qualitative neural model in Ref. [29]. This model comprises a thalamic network consisting of identical thalamocortical (TC) and reticular (RE) neurons, as well as a cortical network corresponding to the unified network model introduced in Ref. [26]. The thalamic and cortical networks are interconnected through weakly coupled neurons. Research has indicated that external high-frequency stimulation can enhance the activity of slow spindles, thereby contributing to improved memory performance.[30] To elucidate the coordination between slow oscillations and sharp-wave ripples, Ghorbani developed a class of hippocampal–cortical–thalamic (HTC) models based on the previously established cortical–thalamic model. The three groups of nuclei are weakly interconnected, with the hippocampal network comprising a neuronal structure analogous to that of the cortical network.[31] The study demonstrated that during the active phase of cortical slow oscillations (SOs), thalamic spindles induced by high volumes of neural signals originating from the corticothalamic interface exhibit prolonged duration and increased amplitude.[32] Girardeau *et al.*[33] and Colgin[34] demonstrated that the neural memory system is highly sensitive to the self-connection parameters of cortical excitatory neurons. Even a minor alteration in self-connection strength can substantially affect the stability of the hippocampal–cortical network, membrane potential oscillation patterns and the incidence of SWRs. This finding is consistent with experimental studies and theoretical models highlighting the critical role of recurrent inhibitory connections within the CA3 circuit in supporting memory replay and consolidation. Specifically, self-connection strength modulates the frequency, amplitude and duration of SWRs by regulating local discharge synchrony and network plasticity. These dynamic characteristics are well established as key neurophysiological substrates underlying memory encoding and consolidation.[33] Various effective stimulation methods are employed in neural networks, such as optogenetic stimulation, acoustic stimulation, electrical stimulation and magnetic stimulation.[35–39] Moreover, numerous physiological experiments have demonstrated that appropriate brain stimulation can enhance memory consolidation.[40–43] In Ref. [44], Fan *et al.* applied external stimulation to the above HTC model and proposed a non-invasive method involving transcranial magnetic and ultrasound stimulation. This study offered a new approach for managing memory disorders. Dynamical analysis of memory models facilitates a deeper understanding of the underlying mechanisms and thereby contributes to further qualitative analysis and control of the model.

Previous research on memory consolidation has predominantly employed experimental methodologies, whereas in-depth analyses of rhythm evolution mechanisms in memory models from the perspective of bifurcation dynamics remain relatively limited. Several characteristic indicators have been identified that contribute to memory consolidation, among which the number of SWRs is a significant indicator. Building upon existing research on neural memory models and without loss of generality, we investigated the evolutionary mechanism of SWRs and the role of cortical self-connection parameters in memory processes within a mature cortico–cortical neural network model from the perspective of bifurcation dynamics. This research primarily proceeds along two dimensions. At the dynamical level, we investigate the impact of self-connection parameters on memory activity within a well-established hippocampal–cortical neural network model from the perspective of bifurcation dynamics. Based on the theoretical framework of nonlinear dynamics, the stability transitions of equilibrium points and the periodic evolution of limit cycles are analyzed through bifurcation analysis. In particular, the parameters of self-coupling connections of excitatory neurons in the cortical region of the model are investigated for their impact on various bifurcation types, including saddle-node bi-

furcation, Hopf bifurcation, period-doubling bifurcation and torus bifurcation. The above analysis is utilized to elucidate the generation mechanisms of brain neural firing activities, including the observed equilibrium state, periodic oscillations or quasi-periodic discharges in the system. At the level of rhythmic characteristics, we first employ an SWR detection algorithm that integrates time–frequency analysis with morphological feature extraction. Through the construction of a recognition framework incorporating parameters such as amplitude envelope, duration and frequency, specific SWR phenomena and characteristic features occurring in the hippocampus are automatically identified from numerical data. Secondly, by integrating bifurcation diagrams observed during system parameter changes with extremum diagrams of neuronal membrane potential oscillations, we summarize and analyze the rhythm transition mechanisms of neural population activities across different dynamical states. Thus, a correlation mechanism linking changes in neuronal self-coupling parameters to the evolution of rhythmic characteristics is established, providing a theoretical foundation for the dynamical behavior observed during memory consolidation.

The structure of this paper is outlined as follows. Section 2 presents an introduction to the memory model. In Section 3, the dynamical mechanism of the model is analyzed by investigating membrane potential changes of hippocampal CA3 excitatory neurons through one-parameter bifurcation diagrams, and the temporal evolution of membrane potential is assessed with heatmaps illustrating changes in SWR counts. Section 4 summarizes the findings and discusses the theoretical and functional implications of these results.

2. Model description

This section provides a detailed description of the hippocampal–cortical memory model. The model is formulated as a high-dimensional system comprising twelve ordinary differential equations. A detailed description of the model is provided below:

$$\frac{\mathrm{d}V_q^k}{\mathrm{d}t} = -\frac{V_q^k}{\tau_q} - x_n N_i^{k_n} P_{iq_n}^{k_n} J_{iq_n}^{k_n} r(V_{q_n}^{k_n}) + \sum_{m=1}^{3} x_m N_{\mathrm{e}}^{k_m} P_{\mathrm{ee}}^{k_{m1}} J_{\mathrm{ee}}^{k_{m1}}(c^k) r(V_{\mathrm{e}}^{k_m}), \tag{1}$$

$$\frac{\mathrm{d}c^k}{\mathrm{d}t} = -\frac{c^k}{\tau_{\mathrm{c}}} + \sum_{n=1}^{3} y_n N_{\mathrm{e}}^{k_n} P_{\mathrm{ee}}^{k_{n1}} \Delta c^k r(V_{\mathrm{e}}^{k_n}). \tag{2}$$

The parameters of the above model are defined as follows: V_q^k represents the membrane potential, and c^k is the adaptation variable of neuron k, where $k \in \{\mathrm{CA3}, \mathrm{CA1}, \mathrm{CX1}, \mathrm{CX2}\}$. τ_{c} denotes the adaptation time constant, which is significantly greater than the membrane time constant τ_q ($q \in \{\mathrm{e},\mathrm{i}\}$) for excitatory and inhibitory neurons. The connection indicators satisfy $x_n, x_m, y_n \in \{0,1\}$ for $n = 1,2,3$ and $m = 1,2,3$, taking the value -1 when a neuronal connection occurs and 0 otherwise.

The population parameters include $N_{j_m}^{k_{m1}}$, $N_{\mathrm{e}}^{k_n}$ and $N_{j_n}^{k_{n1}}$ for neuron counts, $P_{j_n i}^{k_n}$, $P_{j_m q}^{k_m}$ and $P_{\mathrm{ee}}^{k_{n1}}$ for connection probabilities, and $J_{j_n i}^{k_n}$ and $J_{j_m q}^{k_m}$ for connection strengths. The firing rate is given by $r(V)$, with Δc^k representing the incremental adaptation variable of neuron k. The index sets are defined by $k_n, k_m \in \{\mathrm{CA1}, \mathrm{CA3}, \mathrm{CX1}, \mathrm{CX2}\}$ and the extended connection sets $k_{n1}, k_{m1} \in \{\mathrm{CA1}, \mathrm{CA3}, \mathrm{CX1}, \mathrm{CX2}, \mathrm{CA3–CA1}, \mathrm{CX1–CA1}, \mathrm{CA1–CX}, \mathrm{CX2–CA3}, \mathrm{CX2–CA1}\}$.

The structural diagram of the memory model (2) is presented in Fig. 1. The types of bifurcations associated with this model and their corresponding labels are summarized in Table 1.

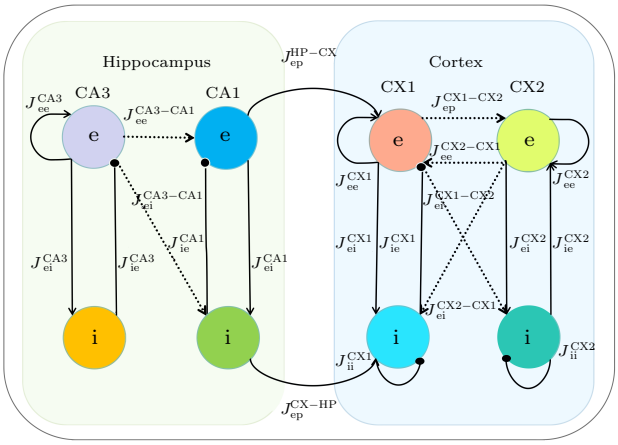


Fig. 1. Structure of synaptic connections in the hippocampal-cortical (HC) network. The hippocampal and cortical subnetworks consist of excitatory neurons (denoted as "e") and inhibitory neurons (denoted as "i"), with the connection strength between each pair of neurons represented by "J". Excitatory synaptic connections are illustrated by arrows, whereas inhibitory connections are depicted by line segments with filled circles at their termini. Short-range connections are represented by solid lines, while long-range connections are indicated by dashed lines. The parameter "p" ($p \in \{\mathrm{e},\mathrm{i}\}$) denotes the receptor network.

Table 1. Bifurcation types and the corresponding labels.

Type of bifurcation	Label	Type of bifurcation	Label
Hopf bifurcation	HB	period-doubling bifurcation	PD
Limit point bifurcation of cycles	LPC	Torus bifurcation	TR

3. Main results

In the hippocampal–cortical memory model (2), the dynamical state of excitatory neurons in the hippocampal CA3 region — including the oscillation frequency and amplitude of their membrane potentials, as well as their connectivity indices with other neuronal populations — may influence the temporal evolution of sharp-wave ripples (SWRs), thereby affecting the process of memory consolidation. Building on this observation, we investigate how the self-connection parameters of cortical excitatory neurons shape both the generation mechanism and the evolutionary pattern of hippocampal CA3 SWRs.

In this section, the self-connection strength of cortical excitatory neurons, denoted by J_{ee}^{CX1}, is fixed, and the bifurcation structure of model (2) as well as the corresponding waveform evolution under these parameter conditions are systematically analyzed.

3.1. Firing mechanism of hippocampal neurons with $J_{ee}^{CX1} = 0.55$

Here, we fix the self-connection strength of the first cortical excitatory population as $J_{ee}^{CX1} = 0.55$ and investigate the dynamical behavior and evolution of SWRs associated with the membrane potential of hippocampal CA3 excitatory neurons as the cortical self-connection probability P_{ee}^{CX1} varies.

3.1.1. One-parameter bifurcation analysis with respect to P_{ee}^{CX1}

We first analyze the dynamical behavior of model (2) in response to changes in the parameter P_{ee}^{CX1}, with particular attention to the resulting bifurcation phenomena. In addition, a heatmap illustrating the variation in the number of SWRs near the fixed self-connection strength $J_{ee}^{CX1} = 0.55$ is computed, and the corresponding results are presented in Fig. 2.

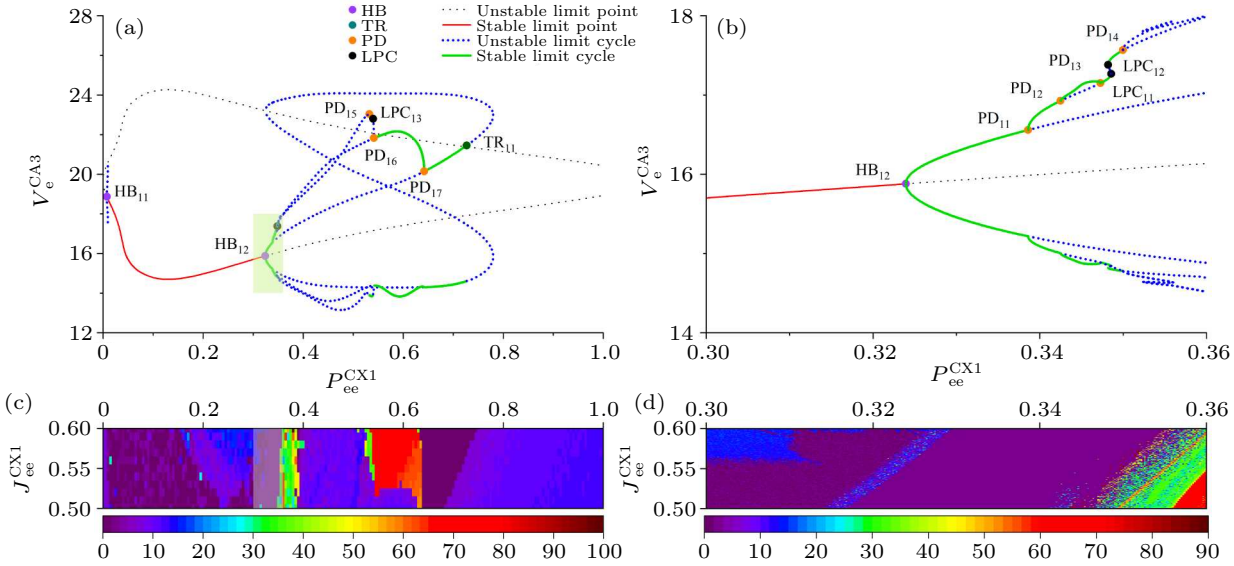


Fig. 2. Bifurcation diagram and heatmap illustrating SWRs. Left: Bifurcation diagram of the model (2) with respect to the parameter $P_{ee}^{CX1} \in [0,1]$ at a fixed value of $J_{ee}^{CX1} = 0.55$, accompanied by a heatmap illustrating SWRs. In the bifurcation diagram, Hopf bifurcations are indicated by purple dots, torus bifurcations by dark green dots, period-doubling bifurcations by yellow dots, and limit point bifurcations of cycles by black dots. Unstable equilibrium points are represented by black dashed lines, stable equilibrium points by red solid lines, unstable limit cycles by thick blue dashed lines, and stable limit cycles by thick green dashed lines. The heatmap illustrates variation in the number of SWRs, with the color transitioning from dark blue to dark red as the number increases. Right: Magnified view of the bifurcation diagram and SWR heatmap within the light green region ($P_{ee}^{CX1} \in [0.30, 0.36]$) from the left diagram. The representation is consistent with that in the left panel.

Figure 2 illustrates the bifurcation types and the corresponding values of P_{ee}^{CX1} at the bifurcation points, as summarized in Table 2.

Table 2. Bifurcation types and Values of P_{ee}^{CX1} as $J_{ee}^{CX1} = 0.55$.

Label	Value of P_{ee}^{CX1}	Label	Value of P_{ee}^{CX1}	Label	Value of P_{ee}^{CX1}
HB_{11}	0.007570659	HB_{12}	0.3239123	PD_{11}	0.3385799
PD_{12}	0.3424808	PD_{13}	0.3472751	LPC_{11}	0.3481935
LPC_{12}	0.3485474	PD_{14}	0.3499633	PD_{15}	0.5322468
LPC_{13}	0.5396592	PD_{16}	0.5420453	PD_{17}	0.6418856
TR_{11}	0.7797442	–	–	–	–

First, we provide a detailed analysis of the bifurcation phenomena identified in Fig. 2. At the bifurcation point HB_{11}, the system undergoes a subcritical Hopf bifurcation, in which an unstable equilibrium point transitions to a stable state while an unstable limit cycle simultaneously emerges. When the parameter P_{ee}^{CX1} lies in the interval (HB_{11}, HB_{12}), the system exhibits the coexistence of stable and unstable equilibrium points. At HB_{12}, the system undergoes a supercritical Hopf bifurcation, where a stable equilibrium point becomes unstable and a stable limit cycle emerges.

As the parameter P_{ee}^{CX1} increases, the system undergoes a period-doubling bifurcation at PD_{11}, resulting in the emergence of a stable limit cycle with larger amplitude and an unstable limit cycle with smaller amplitude. With further increases in P_{ee}^{CX1}, a second period-doubling bifurcation occurs at PD_{12}, again producing a larger amplitude stable limit cycle and a smaller amplitude unstable limit cycle. At PD_{13}, the third period-doubling bifurcation takes place, during which the larger amplitude unstable limit cycle merges with the stable limit cycle, forming a single stable cycle. At this critical point, the system exhibits coexistence between a stable limit cycle and an unstable limit cycle.

As P_{ee}^{CX1} continues to increase, the sole stable limit cycle loses stability due to a limit point bifurcation of cycles at LPC_{11}, leading to the reappearance of an unstable cycle. At

LPC_{12}, another limit point bifurcation of cycles occurs, altering the stability of the limit cycle. The larger amplitude limit cycle regains stability, its amplitude continues to grow, and it still encloses the same small-amplitude unstable limit cycle. At PD_{14}, the system enters a regime in which multiple unstable limit cycles coexist with increasing amplitudes.

With further increases in P_{ee}^{CX1}, the fifth period-doubling bifurcation occurs at PD_{15}, resulting in the formation of a stable limit cycle. Subsequently, at LPC_{13}, the third limit point bifurcation of cycles takes place, destabilizing the previously stable limit cycle. At PD_{16}, another period-doubling bifurcation occurs, during which two unstable limit cycles merge into a single stable limit cycle. The amplitude of the stable limit cycle initially increases and then decreases, eventually converging with the small-amplitude unstable limit cycle at the period-doubling bifurcation point PD_{17}, where the two cycles merge into a single cycle that evolves into a stable state. At TR_{11}, the system undergoes a torus bifurcation, resulting in the loss of stability of the stable limit cycle.

3.1.2. Analysis of rhythmic variation

By incorporating the neuronal rhythm variation graph, we conduct a detailed analysis of the dynamical mechanisms near each bifurcation point and the generation patterns of SWRs during the discharge activity of hippocampal CA3 excitatory neurons.

When the parameter P_{ee}^{CX1} approaches the Hopf bifurcation point HB_{12}, the evolution of the membrane potential of hippocampal CA3 excitatory neurons is illustrated in Fig. 3. The neuronal firing activity begins to exhibit periodic oscillations arising from the equilibrium state, characterized by a relatively smooth transition. Notably, no sharp wave ripples are detected during this phase.

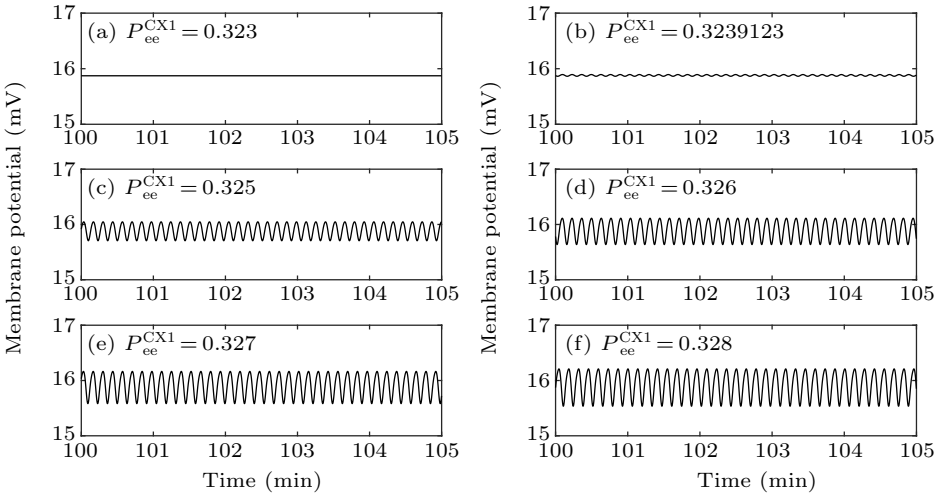


Fig. 3. Rhythmic diagram of V_e^{CA3} near the bifurcation point HB_{12}, with other parameter values listed in Table A1.

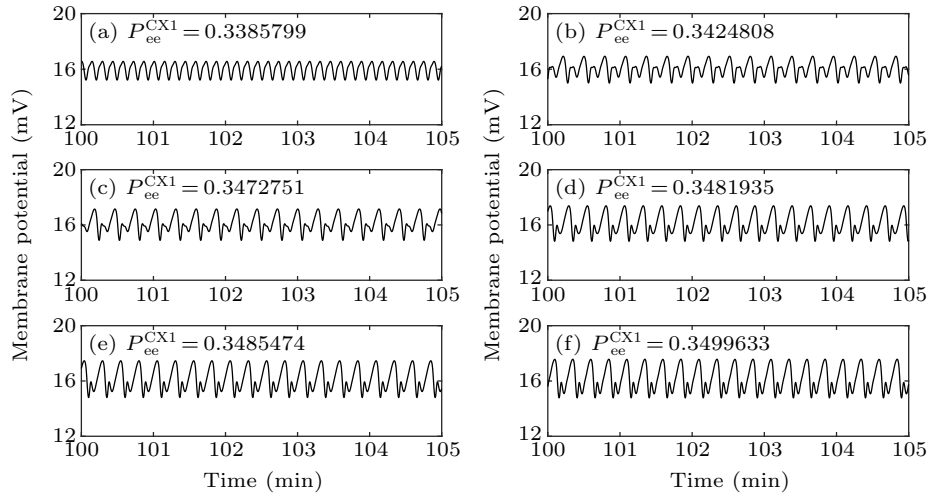


Fig. 4. Rhythmic diagram of V_e^{CA3} corresponding to the parameter P_{ee}^{CX1} near the bifurcation points PD_{11}–PD_{14} and LPC_{11}, LPC_{12}.

As the parameter P_{ee}^{CX1} crosses the bifurcation points PD_{11}–PD_{14}, LPC_{11} and LPC_{12}, Fig. 4 illustrates the corresponding changes in the neuronal membrane potential and the characteristics of SWR rhythms. As shown in Fig. 4, although the oscillations of the neuronal membrane potential gradually change with increasing P_{ee}^{CX1} due to the occurrence of period-

doubling bifurcations, that is, a general increase in amplitude accompanied by a corresponding change in frequency, no sharp wave ripples emerge during this process. These findings indicate that the synchronous amplitude variation of V_e^{CA3} and the spike-peak–to–trough duration of the membrane potential, induced by changes in the self-connection probability P_{ee}^{CX1}, may not satisfy the conditions required for generating SWRs.

As the parameter falls within the range between bifurcation points PD_{14} and PD_{15}, the evolution of the neuronal membrane potential and the characteristics of the SWR rhythm are illustrated in Fig. 5. To more effectively highlight the occurrence of SWRs, red boxes are employed in the full-text rhythm graph to mark ripple waves, which serve as indicators of SWR generation. In this parameter interval, the system enters a state characterized by the coexistence of multiple unstable limit cycles, in which the amplitudes of the limit cycles show a substantial increase as P_{ee}^{CX1} increases. At this stage, the firing activity of the neurons is marked by pronounced spike states, accompanied by a significant increase in the peak–valley distance. Sharp wave ripples emerge, exhibiting a trend in which the number of SWRs first increases and then gradually decreases.

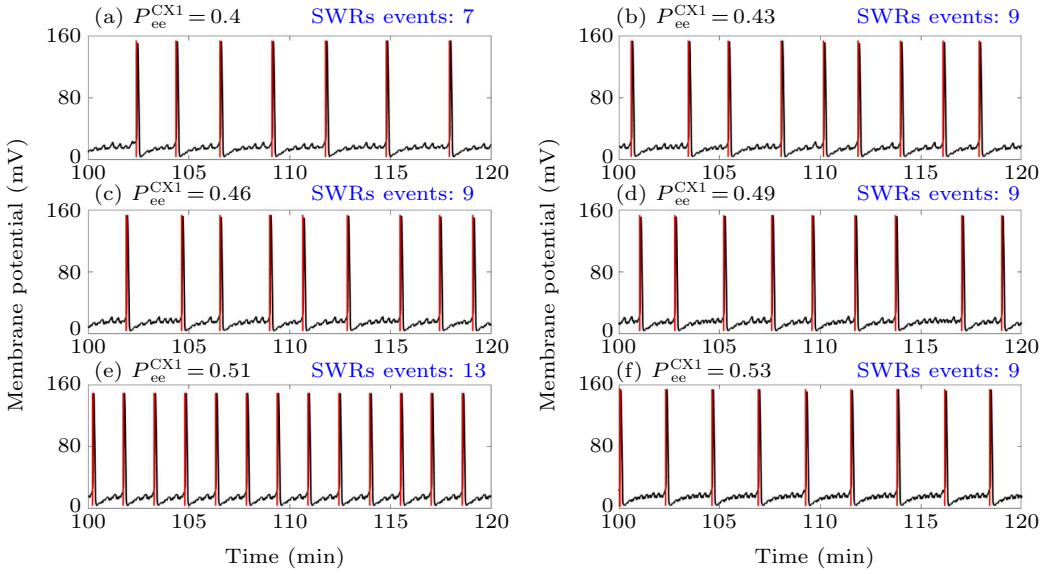


Fig. 5. Rhythmic diagram of V_e^{CA3} in the left neighborhood of the bifurcation point PD_{15}. The generation of SWRs in this figure is highlighted with red rectangular boxes.

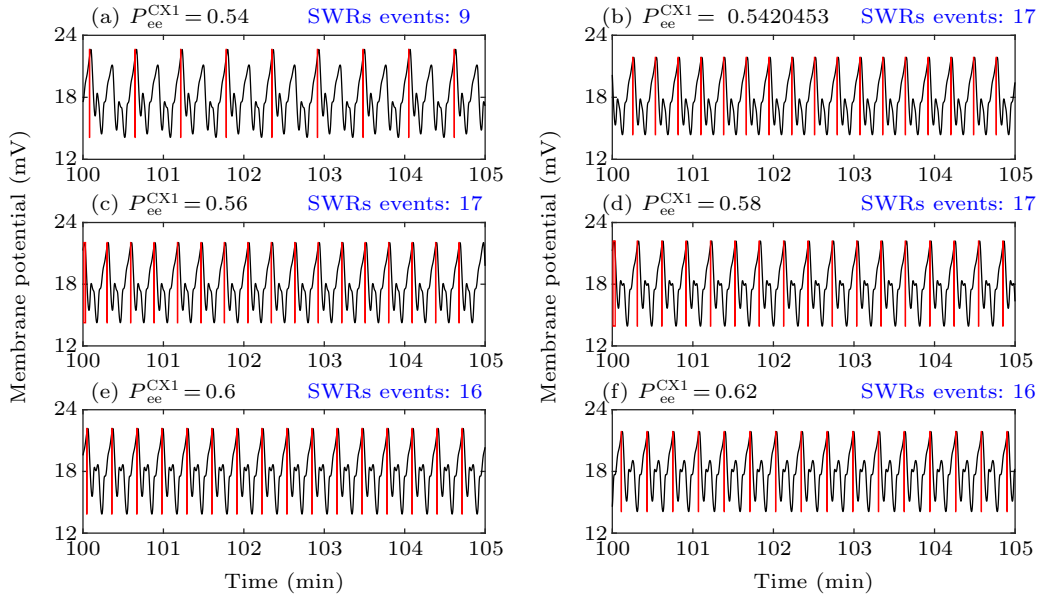


Fig. 6. Rhythmic diagram of V_e^{CA3} in the right neighborhood of the bifurcation point PD_{15}, annotated with SWR markers.

Figure 6 illustrates the evolution of membrane potential and the characteristics of SWR rhythms in the parameter range bounded by the bifurcation points LPC_{13} and PD_{17}. As P_{ee}^{CX1} continues to increase, the system remains in a state characterized by multiple nested limit cycles. At this stage, the amplitude of the membrane potential exceeds that observed in

Fig. 3, accompanied by the emergence of a spiking state. The distance and duration between peaks and troughs satisfy the conditions required for the generation of SWRs, and the number of SWRs exhibits an initial increase followed by a subsequent decline.

In Fig. 2, the one-parameter bifurcation diagram shows a torus bifurcation occurring at TR_{11}. The associated time series and phase portraits are displayed in Fig. 7. The magnified view on the right highlights the phase dynamics during the small-amplitude oscillations of the neuronal membrane potential. Compared with the smaller-amplitude periodic orbits shown in Figs. 4 and 6, the trajectory in Fig. 7 exhibits notable structural changes. The system transitions from stable periodic oscillation to complex high-frequency quasi-periodic oscillation, giving rise to more intricate dynamical behavior.

Figure 8 illustrates the characteristic diagram of the SWR rhythm near the bifurcation point TR_{11}. As shown in Fig. 7, the topological structure of the system remains unchanged near this bifurcation point, resulting in a relatively stable total number of SWRs.

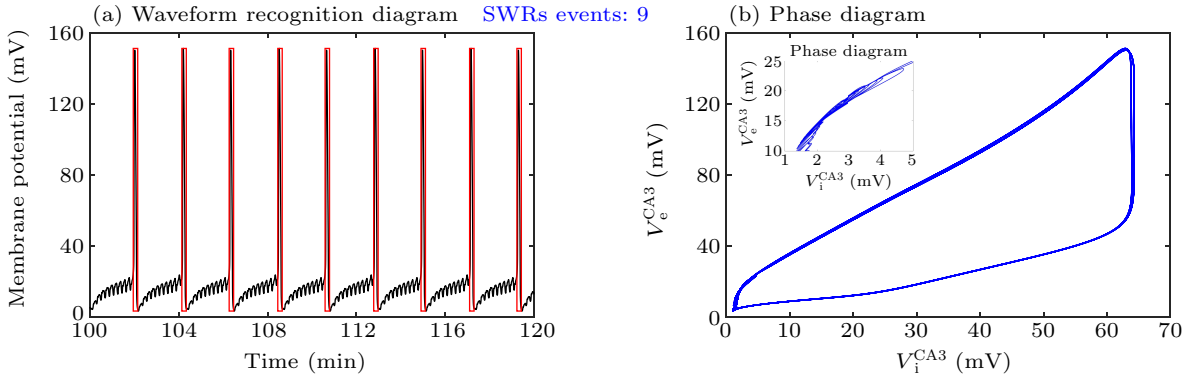


Fig. 7. Rhythmic activity and SWR detection diagrams of V_e^{CA3} with respect to P_{ee}^{CX1}. (a) Rhythmic diagram at TR_{11}, annotated with SWR markers for V_e^{CA3}. (b) Phase diagram corresponding to the parameter value in the region identified in the left diagram, with an expanded view of the low-amplitude range displayed in the upper-left inset.

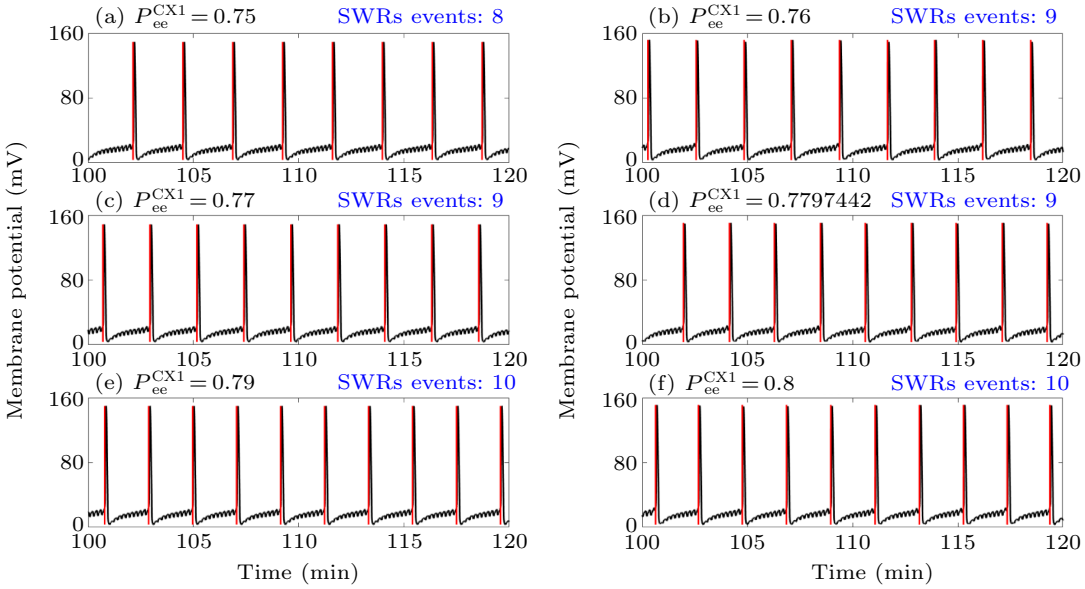


Fig. 8. Rhythmic diagram of the left neighborhood near the bifurcation point TR_{11}, annotated with SWR markers for V_e^{CA3}.

3.1.3. Extremum analysis of neuronal membrane potential

We extracted the maximum and minimum values of the membrane potential from excitatory neurons in the hippocampal CA3 region within the range of the self-connection probability $P_{ee}^{CX1} \in (0.3, 0.8)$ and constructed the corresponding extremum map for this region, as illustrated in Fig. 9. The neuronal firing activity exhibits diverse evolution as the parameter P_{ee}^{CX1} changes. The system begins in a stable discharge state. As bifurcation phenomena emerge, the firing activity of the neuronal membrane potential gradually intensifies, leading to periodic oscillations with progressively increasing amplitude. With further increases in P_{ee}^{CX1}, the system evolves into a high-amplitude oscillatory state characterized by pronounced periodic discharge behavior. By integrating rhythm analysis and waveform recognition, we conclude that within the PD_{14}–

PD_{15} interval, the strength of neuronal self-connection induces complex bifurcation phenomena. Multiple period-doubling bifurcations give rise to multiple nested limit cycles, resulting in oscillatory behavior of the membrane potential. However, as evidenced by the extremum map, small-amplitude oscillations fail to meet the criteria required for the generation of SWRs. As P_{ee}^{CX1} increases further, the amplitude of the membrane potential rises, and the periodic oscillatory behavior induced by complex bifurcation phenomena may lead to the formation of SWRs. With continued increases in P_{ee}^{CX1}, the discharge pattern of the neuronal membrane potential exhibits greater variability, indicating the sensitivity of the system to parametric variations.

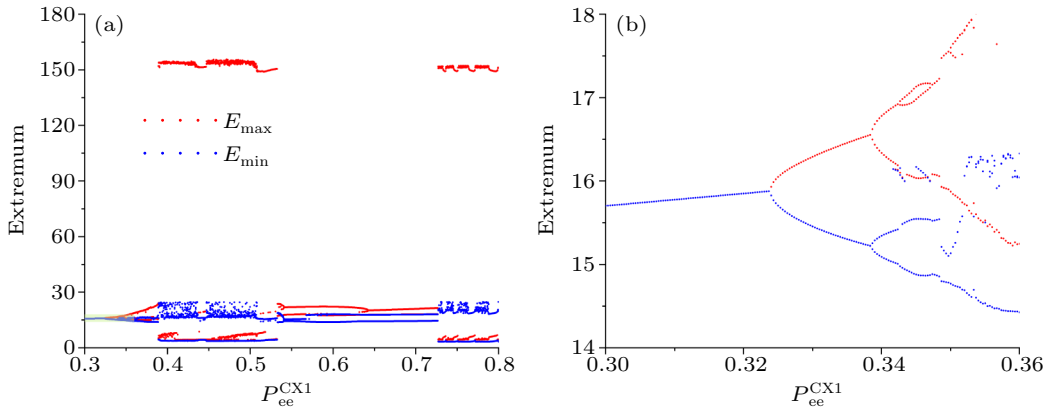


Fig. 9. Extrema diagram of the membrane potential V_e^{CA3} with respect to P_{ee}^{CX1}. (a) Extrema diagram of V_e^{CA3} for $P_{ee}^{CX1} \in (0.3, 0.8)$. Maximum values of the neuronal membrane potential are marked by red dots, and minimum values are marked by blue dots. (b) Enlarged view of the green-shaded region corresponding to $P_{ee}^{CX1} \in (0.30, 0.36)$ in the left diagram.

3.2. Firing mechanism of hippocampal neurons with $J_{ee}^{CX1} = 1.0$

In this section, we fix the self-connection strength of the first excitatory neuron in the cortex at $J_{ee}^{CX1} = 1.0$, and investigate the dynamical behavior and evolutionary patterns of SWRs associated with the membrane potential of excitatory neurons in the hippocampal CA3 region as the cortical excitatory neuron self-connection probability P_{ee}^{CX1} varies.

3.2.1. One-parameter bifurcation analysis with respect to P_{ee}^{CX1}

First, we analyze the dynamical behavior of model (2) in response to the parameter P_{ee}^{CX1}, with a particular focus on the associated bifurcation phenomena. Then, a heatmap depicting changes in the number of SWRs near the self-connection strength $J_{ee}^{CX1} = 1.0$ is generated, and the two corresponding graphs are presented in Fig. 10.

Figure 2 illustrates the types of bifurcation and the corresponding values of P_{ee}^{CX1} at the bifurcation points, as shown in Table 3.

Table 3. Bifurcation types and values of P_{ee}^{CX1} as $J_{ee}^{CX1} = 1.0$.

Label	Value of P_{ee}^{CX1}	Label	Value of P_{ee}^{CX1}	Label	Value of P_{ee}^{CX1}
HB_{21}	0.004107808	HB_{22}	0.06214856	PD_{21}	0.07040077
PD_{22}	0.07250708	PD_{23}	0.07395214	TR_{21}	0.0767026
TR_{22}	0.08000623	PD_{24}	0.08527067	PD_{25}	0.1011775
PD_{26}	0.1014247	TR_{23}	0.1032142	HB_{23}	0.2752843
HB_{24}	0.3642840	PD_{27}	0.3882965	PD_{28}	0.3950402
PD_{29}	0.4707080	PD_{210}	0.4784027	LP_{21}	0.5013242

First, we analyze the shaded region in the left panel of the one-parameter bifurcation diagram in Fig. 10, corresponding to the magnified view in the right panel. At the bifurcation point HB_{22}, the system undergoes a supercritical Hopf bifurcation, in which the stable equilibrium loses stability and a stable limit cycle emerges. As parameters increase, the system undergoes a period-doubling bifurcation at PD_{21}, where a stable large-amplitude limit cycle and an unstable small-amplitude limit cycle emerge. As P_{ee}^{CX1} increases further, the system experiences a second period-doubling at PD_{22}, where the larger stable limit cycle bifurcates into a large-amplitude stable and small-amplitude unstable limit cycle, enclosing other small-amplitude unstable cycles. At the third period-doubling PD_{23}, the stable limit cycle and large-amplitude unstable cycle coalesce into a single stable limit cycle, while the small-amplitude unstable cycle remains unstable. As P_{ee}^{CX1} continues to increase, a torus bifurcation occurs at TR_{21}, destabilizing the stable limit cycle. At TR_{22}, the second torus bifurcation occurs, with the large-amplitude unstable cycle evolving into a stable state. At PD_{24}, the large-amplitude limit cycle loses stability, forming two unstable limit cycles. As P_{ee}^{CX1} further increases, the amplitude of the unstable limit cycle first rises, then decreases. At PD_{25}, a stable limit cycle emerges and merges with the small-amplitude unstable limit cycle at PD_{26}, entering a transient stable phase. Finally, at TR_{23}, a torus bifurcation occurs, causing the limit cycle to lose stability.

Then, we explore the bifurcation phenomena occurring outside the shaded region. As P_{ee}^{CX1} crosses the Hopf bifurcation point HB_{21}, the system undergoes a subcritical Hopf bifurcation, during which the equilibrium point transitions from

an unstable state to a stable state. When the parameter lies in the interval (HB_{21}, HB_{22}), the system exhibits coexistence of both stable and unstable equilibrium points. At HB_{23}, the system undergoes another subcritical Hopf bifurcation, whereby the unstable equilibrium point transitions to a stable state and an unstable limit cycle emerges. As the parameter increases within the interval (HB_{23}, HB_{24}), the amplitude of the stable limit cycle gradually grows. At HB_{24}, the system undergoes a supercritical Hopf bifurcation, resulting in the transition from a stable equilibrium point to an unstable state and the simultaneous emergence of a stable limit cycle. Throughout this process, the large-amplitude unstable limit cycle persists. As P_{ee}^{CX1} continues to increase, the seventh period-doubling bifurcation occurs at PD_{27}, where a stable limit cycle bifurcates into a larger-amplitude stable limit cycle and a smaller-amplitude unstable limit cycle. At PD_{28}, another period-doubling bifurcation occurs, leading to the splitting of the stable limit cycle into two unstable limit cycles and resulting in the coexistence of multiple limit cycles. As P_{ee}^{CX1} continues to increase, a stable limit cycle emerges at PD_{29}, which merges with a small-amplitude unstable limit cycle at PD_{210} to form a single stable limit cycle. At LP_{21}, the limit cycles disappear.

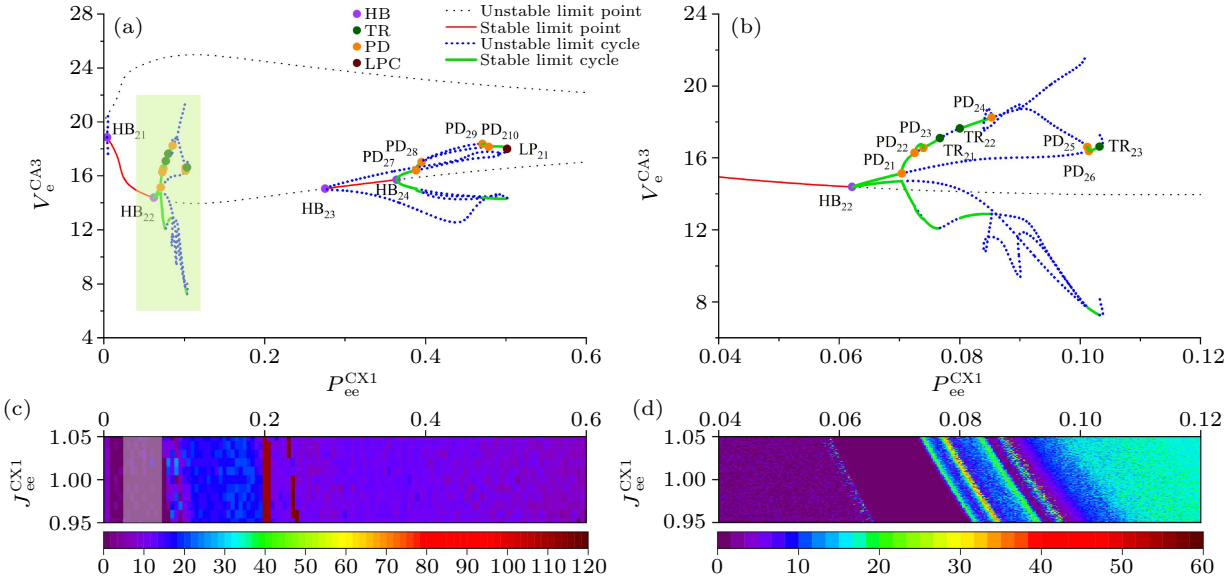


Fig. 10. Bifurcation diagram and heatmap illustrating SWRs. (a) Bifurcation diagram of the model (2) with respect to the parameter $P_{ee}^{CX1} \in [0,1]$ at a fixed value of $J_{ee}^{CX1} = 1.0$, accompanied by a heatmap illustrating SWRs. In the bifurcation diagram, Hopf bifurcations are indicated by purple dots, torus bifurcations by dark green dots, period-doubling bifurcations by yellow dots, and limit points by brown dots. Unstable equilibrium points are represented by black dashed lines, stable equilibrium points by red solid lines, unstable limit cycles by thick blue dashed lines, and stable limit cycles by thick green dashed lines. The heatmap illustrates the variation in the number of SWRs. As the number increases, the color transitions from dark blue to dark red. (b) Magnified view of the bifurcation diagram and the SWR heatmap within the light green region ($P_{ee}^{CX1} \in [0, 0.6]$) from the left diagram. The representation is consistent with that in the left panel.

3.2.2. Analysis of rhythmic variation

Furthermore, by integrating the neuronal rhythm variation graph, we conduct a detailed analysis of the dynamical mechanism near each bifurcation point, as well as the generation patterns of SWRs during the discharge activity of excitatory neurons in the CA3 region of the hippocampus.

When the parameters cross the supercritical Hopf bifurcation point HB_{22}, the neuronal state begins to evolve from the original equilibrium point to an oscillatory regime, accompanied by the emergence of steady periodic behavior of the neuronal membrane potential. No sharp wave ripples are detected near the bifurcation point HB_{22}. The corresponding rhythmic characteristic diagram is presented in Fig. 11.

When P_{ee}^{CX1} crosses the period-doubling bifurcation points PD_{21}–PD_{24} and the torus bifurcation points TR_{21} and TR_{22}, the neuronal membrane potential exhibits periodic oscillations. As P_{ee}^{CX1} increases, the amplitude of these oscillations progressively rises. The overall variation of the membrane potential tends toward stabilization. Since the amplitude changes induced by variation of the self-connection probability P_{ee}^{CX1} fail to meet synchronization criteria, and the spike-peak-to-trough distance and duration of the neuronal membrane potential do not satisfy the requirements for sharp wave ripple generation, no sharp wave ripples are produced. The corresponding rhythmic diagram in this parameter region is illustrated in Fig. 12.

The time series and phase diagrams corresponding to the bifurcation point TR_{23} are presented in Fig. 13. As shown in the one-parameter bifurcation diagram in Fig. 10, the system undergoes a torus bifurcation at TR_{23}. Compared to the stable trajectory depicted in Fig. 11 and the oscillatory trajectory illustrated in Fig. 12, the trajectory in Fig. 13 demonstrates a significant structural transformation. This indicates that the

periodic orbit of the neuronal membrane potential rhythm no longer maintains a single frequency, but instead evolves from a simple periodic orbit to a complex quasi-periodic orbit containing multiple amplitude and frequency components. This transition signifies the emergence of more intricate dynamical behavior in the system.

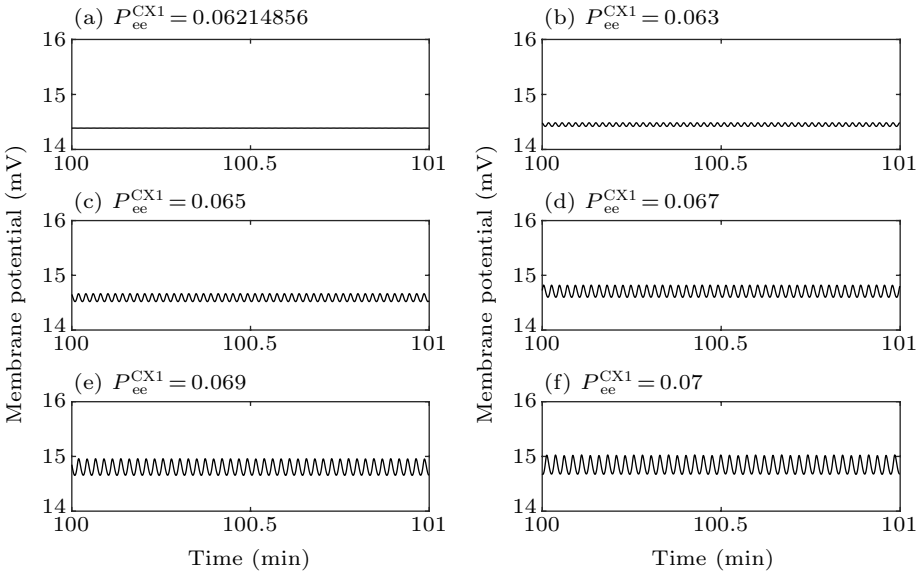


Fig. 11. The rhythmic diagram of V_e^{CA3} near the bifurcation point HB_{22}, where other parameter values are listed in Table A1.

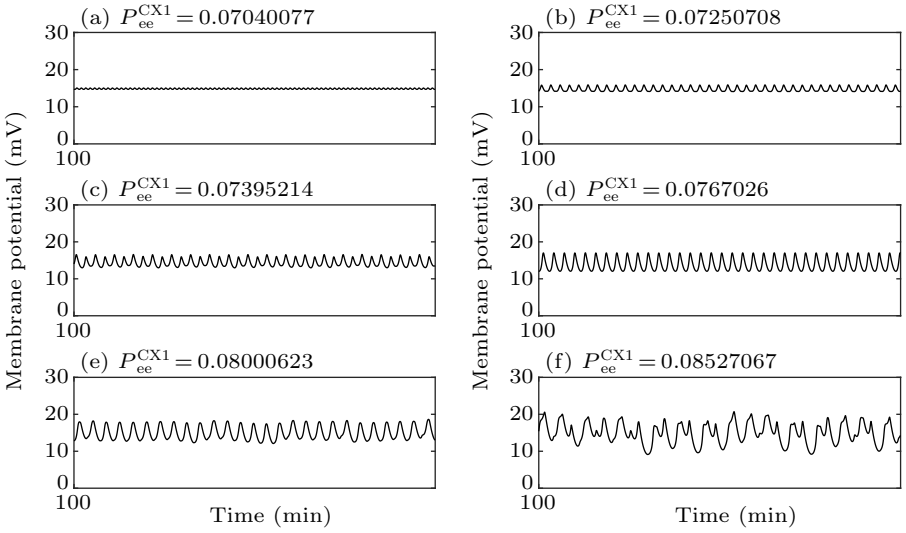


Fig. 12. The rhythmic diagram of V_e^{CA3} with respect to P_{ee}^{CX1} near the bifurcation points PD_{21}–PD_{24} and TR_{21}, TR_{22}.

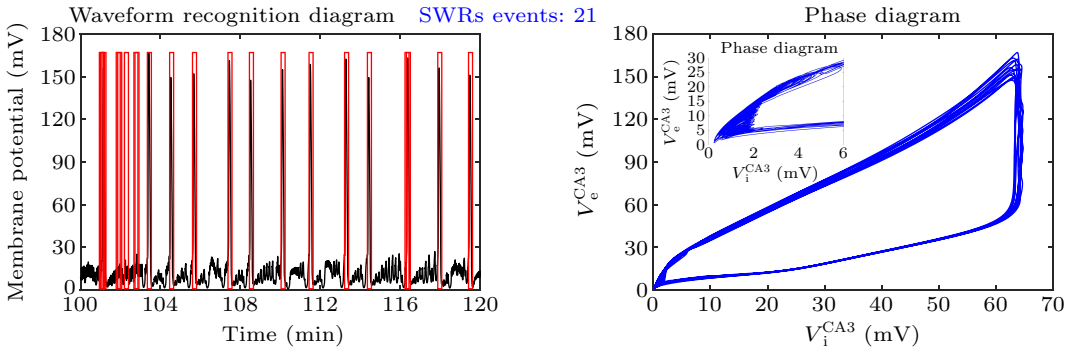


Fig. 13. The rhythmic activity diagram and SWRs detection diagram of V_e^{CA3} with respect to P_{ee}^{CX1}. (a) Rhythmic diagram at TR_{23}, annotated with SWR markers for V_e^{CA3}. (b) Phase diagram corresponding to the parameter value in the respective region identified in the left diagram, with an expanded view of the phase diagram in the low-amplitude range displayed in the upper-left inset.

When P_{ee}^{CX1} passes through the bifurcation region PD_{25}–TR_{23}, the system exhibits coexistence of multiple limit cycles. At this stage, the significant increase in the peak-to-trough distance and the prolonged duration lead to the re-emergence of SWRs. Furthermore, the number of SWRs varies considerably with the parameter values. The corresponding rhythmic diagram near this bifurcation region is illustrated in Fig. 14.

When P_{ee}^{CX1} crosses the bifurcation points HB_{24} and PD_{27}–PD_{210}, the membrane potential continues to exhibit sharp spike discharges and a very high oscillation frequency, leading to the generation of SWRs. Notably, the number of SWRs remains relatively stable within this parameter range. The corresponding rhythmic diagrams near these bifurcation points are illustrated in Fig. 15.

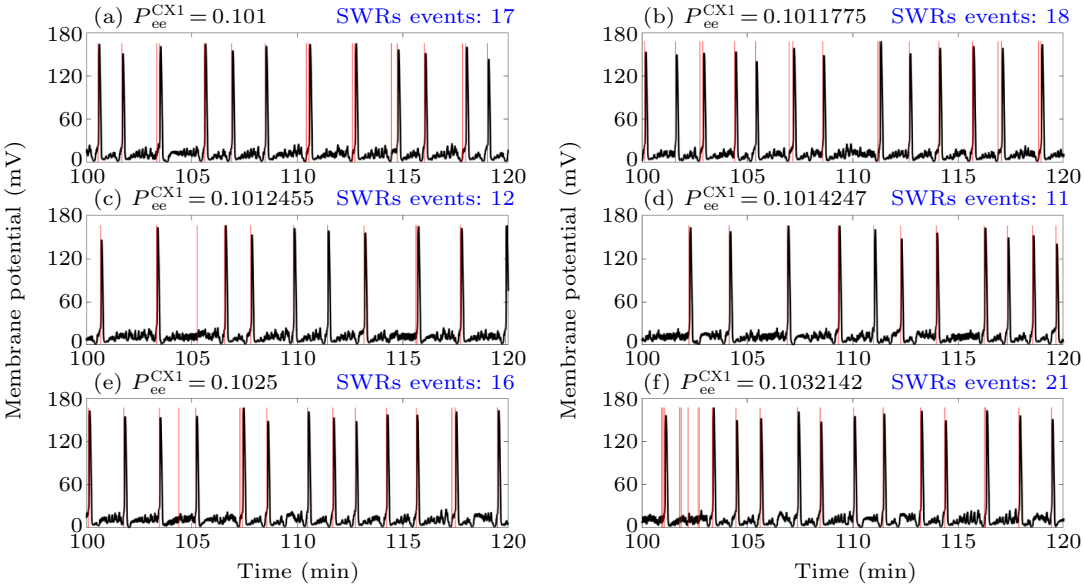


Fig. 14. The rhythmic diagram of the left neighborhood near the bifurcation points PD_{25}–TR_{23}. The generation of SWRs in this figure is highlighted with red rectangular boxes.

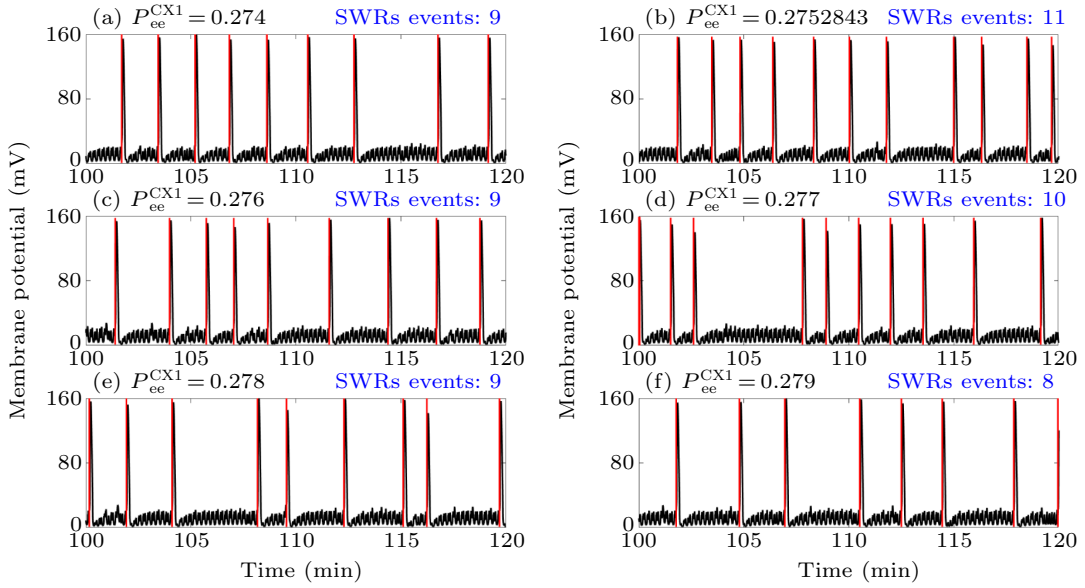


Fig. 15. The rhythmic diagram of the left neighborhood near the bifurcation points HB_{24} and PD_{27}–PD_{210}, annotated with SWRs markers for V_e^{CA3}.

3.2.3. Extremum analysis of neuronal membrane potential

We extracted the maximum and minimum values of the membrane potential from excitatory neurons of the CA3 region in the hippocampus within the range of the self-connection probability $P_{ee}^{CX1} \in (0, 0.6)$ and constructed the corresponding extremum map for this region, as illustrated in Fig. 16. From this figure, we can summarize that the neuronal firing activity undergoes diverse transformations as the parameter P_{ee}^{CX1} gradually increases. Initially, the membrane potential exhibits a brief high-amplitude firing state. As P_{ee}^{CX1} increases, the system evolves into a steady state. A further in-

crease of P_{ee}^{CX1} drives the membrane potential into a periodic oscillatory state, where the excitatory neurons in the CA3 region of the hippocampus exhibit low-amplitude oscillations, characterized by a relatively stable oscillatory firing pattern. As the parameter increases, the system undergoes a period-doubling bifurcation at PD_{21}. As the self-connection probability P_{ee}^{CX1} continues to increase, the amplitude of the membrane potential gradually rises. According to waveform recognition and rhythmic analysis, SWRs begin to emerge in the P_{ee}^{CX1} range between PD_{24} and PD_{25}. As P_{ee}^{CX1} continues to increase, both the oscillation amplitude and the frequency of the membrane potential gradually evolve, leading to diverse discharge behaviors. This process highlights the continuity and sensitivity of neuronal activity to parameter variations.

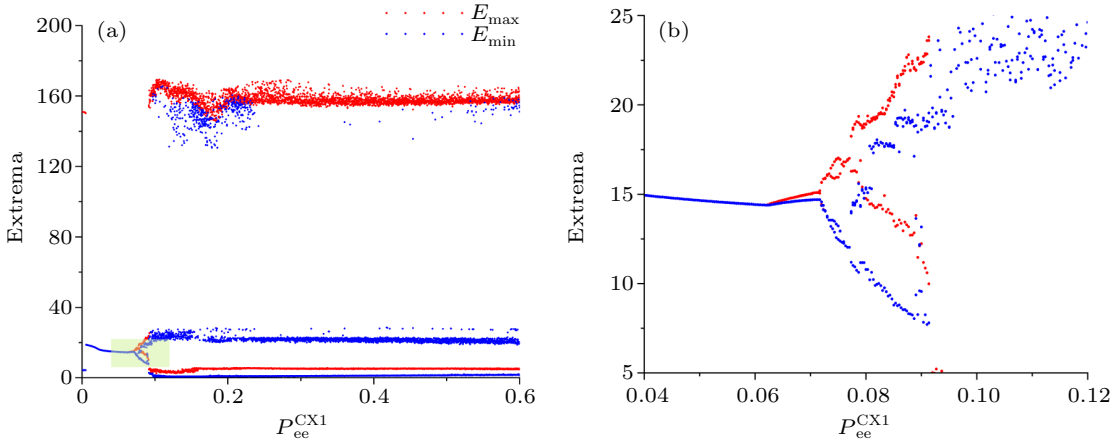


Fig. 16. The extrema diagram of the membrane potential V_e^{CA3} with respect to P_{ee}^{CX1}. (a) The extrema diagram of V_e^{CA3} for $P_{ee}^{CX1} \in (0, 0.6)$. The maximum values of the neuronal membrane potential are marked by red dots and the minimum values by blue dots. (b) An enlarged view of the green-shaded region corresponding to $P_{ee}^{CX1} \in (0.04, 0.12)$ in the left diagram.

4. Discussion and conclusion

This study investigates the hippocampal-cortical memory neural model (Eq. (2)) and focuses on how specific parameters influence the generation mechanisms and evolutionary dynamics of hippocampal SWRs during membrane potential fluctuations of excitatory neurons in the hippocampal CA3 region (V_e^{CA3}). The self-connection strength of cortical excitatory neurons (J_{ee}^{CX1}) is fixed, and the bifurcation behavior of V_e^{CA3}, along with the corresponding waveform evolution trend, is analyzed. The research revealed that the memory model (Eq. (2)) exhibited a variety of bifurcation phenomena, including Hopf bifurcation, period-doubling bifurcation, torus bifurcation, and limit point bifurcation of cycles, as the parameter P_{ee}^{CX1} varies. These bifurcation phenomena reflect the complex nonlinear dynamical characteristics of the high-dimensional model. Based on the rhythm transition mechanisms of neuronal firing activity, we identified the generation and variation patterns of SWRs.

By analyzing the single-parameter bifurcation diagram, we identified the bifurcation points and their surrounding parameter regions. We further investigated the waveforms and dynamic behaviors of excitatory neurons in the hippocampal CA3 region, successfully identifying and extracting hippocampal sharp wave ripples (SWRs) generated during neuronal dynamical evolution. By examining the variation in SWR frequency near each bifurcation point, we found that neuronal rhythms are prone to abrupt transitions at these critical points — conditions favorable for SWR generation. New periodic oscillations are likely to emerge near certain Hopf and period-doubling bifurcation points. When amplitude synchrony and peak-to-peak intervals meet the physiological criteria for SWR generation, sharp wave ripples are triggered. Additionally, changes in system stability near torus bifurcations and saddle-node bifurcations of limit cycles also promote the emergence of SWRs. These findings are consistent with previous research on neural dynamics models, offering a robust theoretical and empirical basis for understanding and modulating memory-related neural oscillations. Furthermore, this study establishes a viable dynamical framework for examining the generation and evolution of SWRs. The results also indicate that the nonlinear bifurcation mechanisms regulated by self-connection parameters may underlie the generation and modulation patterns of hippocampal SWRs.

Additionally, time series analysis reveals that bifurcation occurrence may not always lead to SWR generation. For example, certain low-amplitude oscillations of the membrane potential of excitatory neurons fail to induce SWRs, whereas high-amplitude oscillations are more likely to give rise to such events. Based on this phenomenon, we extracted the maximum and minimum neuronal membrane potential values and constructed corresponding extremum diagrams for these regions. A comparative analysis between the one-parameter bifurcation diagram and the extremum diagram revealed that large-amplitude oscillations of the neuronal membrane potential near bifurcation points are more conducive to the genera-

tion of SWRs.

Finally, a two-parameter bifurcation diagram based on P_{ee}^{CX1} and J_{ee}^{CX1} of excitatory neuron self-connections is presented. This diagram is compared with a heatmap illustrating the variation in SWR counts as a function of P_{ee}^{CX1} and J_{ee}^{CX1}, as shown in Fig. 17, to investigate the relationship between hippocampal SWR generation and underlying bifurcation phenomena. By comparing the two scenarios, it can be concluded that the regions surrounding the key bifurcation points demonstrate high sensitivity to parameter variations, corresponding precisely to those areas where the SWR count exhibits significant fluctuations. Furthermore, the spatial distribution of the SWR count in the heatmap reveals that abrupt changes in SWR frequency within specific parameter ranges indicate the system's transition into a critical or transitional state. By comparing the observed SWR frequencies with physiological data from healthy individuals, a stable operational region within the bifurcation parameter space can be identified. This region supports normal neuronal oscillatory activity while preventing pathological over-synchronization. The boundary of this region is dynamically determined by the oscillation count and provides a robust basis for identifying potential intervention targets and assessing their feasibility.

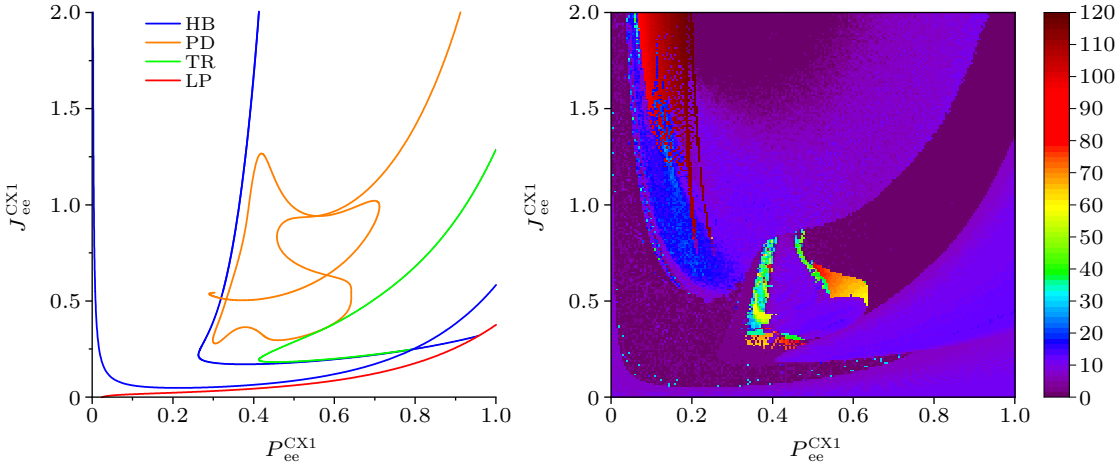


Fig. 17. The two-parameter bifurcation diagram and its corresponding heatmap illustrating the number of SWRs. (a) The two-parameter bifurcation diagram for V_e^{CA3} based on $P_{ee}^{CX1} \in (0,1)$ and $J_{ee}^{CX1} \in (0,2)$. (b) The heatmap depicts the variation in the number of SWRs during the time interval $t \in [100,120]$ (unit: min), with colors transitioning from dark blue to dark red as the count increases. The values of P_{ee}^{CX1} and J_{ee}^{CX1} are maintained as in the left panel, while the remaining parameter values are provided in Table A1.

Building upon this mapping, self-connection parameters that exhibit high sensitivity in hippocampal neuronal circuits can be prioritized as control variables in future applications. Through targeted regulation via synaptic plasticity modulation, pharmacological interventions, or exogenous neuromodulation techniques — including optogenetics, deep brain stimulation, and transcranial electrical stimulation — the strength of self-connections can be precisely modulated to maintain system dynamics within parameter regimes conducive to memory consolidation. From a control-theoretic perspective, bifurcation analysis enables the design of minimal-energy intervention strategies. By integrating sensitivity analysis with stability assessment, subtle and precise perturbations can guide the system toward desired dynamical trajectories. Notably, the dynamical map also facilitates the identification of potential "danger zones," thereby helping to prevent stimulation-induced pathological synchronization. Thus, the integrated two-parameter bifurcation–heatmap analysis presented in this study not only provides a novel framework for elucidating the mechanistic origins of SWRs but also establishes a robust theoretical and methodological foundation for model-driven memory enhancement and neurotherapeutic interventions.

Appendix A: Supplementary table

Table A1. The biological parameters of the hippocampal-cortical neural memory model Ref. [44].

Parameter	Value	Unit	Definition
J_{ee}^{CX1}	[0,2]	mV	Strength of connection from excitatory to excitatory neurons in CX1
P_{ee}^{CX1}	[0,1]	–	Probability of connection from excitatory to excitatory neurons in CX1
τ_e	0.02	s	Membrane relaxation time constant for excitatory neurons
τ_i	0.01	s	Membrane relaxation time constant for inhibitory neurons
τ_c	0.5	s	Adaptation recovery time
r_0	0.1	Hz	Minimum firing rate in completely depolarized state

Table A1. Continued.

Parameter	Value	Unit	Definition
r_1	70	Hz	Maximum firing rate in completely depolarized state
$c_{\max}$	10	mV	Adaptation threshold level
g_c	3	mV	Sharpness of excitatory-excitatory connection dependence on adaptation variable
g_e^{CA3}	6	mV	Sharpness of firing rate dependence on membrane potential from CA3 excitatory neurons
g_i^{CA3}	3	mV	Sharpness of firing rate dependence on membrane potential from CA3 inhibitory neurons
g_e^{CA1}	0.5	mV	Sharpness of firing rate dependence on membrane potential from CA1 excitatory neurons
g_i^{CA1}	0.25	mV	Sharpness of firing rate dependence on membrane potential from CA1 inhibitory neurons
g_e^{CX1}	5	mV	Sharpness of firing rate dependence on membrane potential from CX1 excitatory neurons
g_i^{CX1}	2	mV	Sharpness of firing rate dependence on membrane potential from CX1 inhibitory neurons
g_e^{CX2}	5	mV	Sharpness of firing rate dependence on membrane potential from CX2 excitatory neurons
g_i^{CX2}	2	mV	Sharpness of firing rate dependence on membrane potential from CX2 inhibitory neurons
V_e^{*CA3}	40	mV	Firing threshold potential for excitatory neurons in CA3 region
V_i^{*CA3}	25	mV	Firing threshold potential for inhibitory neurons in CA3 region
V_e^{*CA1}	19	mV	Firing threshold potential for excitatory neurons in CA1 region
V_i^{*CA1}	20	mV	Firing threshold potential for inhibitory neurons in CA1 region
V_e^{*CX1}	30	mV	Firing threshold potential for excitatory neurons in CX1 network
V_i^{*CX1}	30	mV	Firing threshold potential for inhibitory neurons in CX1 network
V_e^{*CX2}	30	mV	Firing threshold potential for excitatory neurons in CX2 network
V_i^{*CX2}	30	mV	Firing threshold potential for inhibitory neurons in CX2 network
J_{ee}^{CA3}	0.7	mV	Base connection strength between excitatory neurons in CA3
J_{ei}^{CA3}	0.3	mV	Connection strength from excitatory to inhibitory neurons in CA3
J_{ie}^{CA3}	0.51	mV	Connection strength from inhibitory to excitatory neurons in CA3
J_{ei}^{CA1}	0.22	mV	Connection strength from excitatory to inhibitory neurons in CA1
J_{ie}^{CA1}	0.87	mV	Connection strength from inhibitory to excitatory neurons in CA1
J_{ii}^{CA1}	0.25	mV	Connection strength between inhibitory neurons in CA1
J_{ei}^{CX1}	0.42	mV	Connection strength from excitatory to inhibitory neurons in CX1
J_{ie}^{CX1}	1.4	mV	Connection strength from inhibitory to excitatory neurons in CX1
J_{ii}^{CX1}	0.3	mV	Connection strength between inhibitory neurons in CX1
J_{ee}^{CX2}	0.38	mV	Base connection strength between excitatory neurons in CX2
J_{ei}^{CX2}	0.48	mV	Connection strength from excitatory to inhibitory neurons in CX2
J_{ie}^{CX2}	1.25	mV	Connection strength from inhibitory to excitatory neurons in CX2
J_{ii}^{CX2}	0.57	mV	Connection strength between inhibitory neurons in CX2
J_{ee}^{CA3CA1}	0.15	mV	Connection strength from CA3 excitatory to CA1 excitatory neurons
J_{ei}^{CA3CA1}	0.04	mV	Connection strength from CA3 excitatory to CA1 inhibitory neurons
J_{ee}^{CX2CA3}	1.88	mV	Connection strength from CX2 excitatory to CA3 excitatory neurons
J_{ei}^{CX2CA3}	0.31	mV	Connection strength from CX2 excitatory to CA3 inhibitory neurons
J_{ee}^{CA1CX1}	2	mV	Connection strength from CA1 excitatory to CX1 excitatory neurons
J_{ei}^{CA1CX1}	1	mV	Connection strength from CA1 excitatory to CX1 inhibitory neurons
J_{ee}^{CX1CA1}	1.04	mV	Connection strength from CX1 excitatory to CA1 excitatory neurons
J_{ei}^{CX1CA1}	0.21	mV	Connection strength from CX1 excitatory to CA1 inhibitory neurons
J_{ee}^{CA1CX2}	2	mV	Connection strength from CA1 excitatory to CX2 excitatory neurons
J_{ei}^{CA1CX2}	1	mV	Connection strength from CA1 excitatory to CX2 inhibitory neurons
J_{ee}^{CX2CX1}	0.67	mV	Connection strength from CX2 excitatory to CX1 excitatory neurons
J_{ei}^{CX2CX1}	1.8	mV	Connection strength from CX2 excitatory to CX1 inhibitory neurons
J_{ee}^{CX1CX2}	0.039	mV	Connection strength from CX1 excitatory to CX2 excitatory neurons
J_{ei}^{CX1CX2}	1.62	mV	Connection strength from CX1 excitatory to CX2 inhibitory neurons
Δ_c^{CA3}	0.0064	–	Average adaptive parameter per incoming action potential in CA3
Δ_c^{CA1}	0.002	–	Average adaptive parameter per incoming action potential in CA1
Δ_c^{CX1}	0.005	–	Average adaptive parameter per incoming action potential in CX1
Δ_c^{CX2}	0.0054	–	Average adaptive parameter per incoming action potential in CX2
P_{ee}^{CA3}	0.25	–	Connection probability between excitatory neurons in CA3
P_{ei}^{CA3}	0.3	–	Connection probability from excitatory to inhibitory neurons in CA3
P_{ie}^{CA3}	0.5	–	Connection probability from inhibitory to excitatory neurons in CA3
P_{ei}^{CA1}	0.3	–	Connection probability from excitatory to inhibitory neurons in CA1
P_{ie}^{CA1}	0.8	–	Connection probability from inhibitory to excitatory neurons in CA1
P_{ii}^{CA1}	0.25	–	Connection probability between inhibitory neurons in CA1
P_{ei}^{CX1}	0.2	–	Connection probability from excitatory to inhibitory neurons in CX1
P_{ie}^{CX1}	0.2	–	Connection probability from inhibitory to excitatory neurons in CX1
P_{ii}^{CX1}	0.2	–	Connection probability between inhibitory neurons in CX1

Table A1. Continued.

Parameter	Value	Unit	Definition
P_{ee}^{CX2}	0.2	–	Connection probability between excitatory neurons in CX2
P_{ei}^{CX2}	0.2	–	Connection probability from excitatory to inhibitory neurons in CX2
P_{ie}^{CX2}	0.2	–	Connection probability from inhibitory to excitatory neurons in CX2
P_{ii}^{CX2}	0.2	–	Connection probability between inhibitory neurons in CX2
P_{ee}^{CA3CA1}	0.6	–	Connection probability from CA3 excitatory to CA1 excitatory neurons
P_{ei}^{CA3CA1}	0.2	–	Connection probability from CA3 excitatory to CA1 inhibitory neurons
P_{ee}^{CX2CA3}	0.02	–	Connection probability from CX2 excitatory to CA3 excitatory neurons
P_{ei}^{CX2CA3}	0.02	–	Connection probability from CX2 excitatory to CA3 inhibitory neurons
P_{ee}^{CA1CX1}	0.002	–	Connection probability from CA1 excitatory to CX1 excitatory neurons
P_{ei}^{CA1CX1}	0.002	–	Connection probability from CA1 excitatory to CX1 inhibitory neurons
P_{ee}^{CX1CA1}	0.03	–	Connection probability from CX1 excitatory to CA1 excitatory neurons
P_{ei}^{CX1CA1}	0.03	–	Connection probability from CX1 excitatory to CA1 inhibitory neurons
P_{ee}^{CA1CX2}	0.002	–	Connection probability from CA1 excitatory to CX2 excitatory neurons
P_{ei}^{CA1CX2}	0.002	–	Connection probability from CA1 excitatory to CX2 inhibitory neurons
P_{ee}^{CX1CX2}	0.01	–	Connection probability from CX1 excitatory to CX2 excitatory neurons
P_{ei}^{CX1CX2}	0.01	–	Connection probability from CX1 excitatory to CX2 inhibitory neurons
P_{ee}^{CX2CX1}	0.01	–	Connection probability from CX2 excitatory to CX1 excitatory neurons
P_{ei}^{CX2CX1}	0.01	–	Connection probability from CX2 excitatory to CX1 inhibitory neurons
N_e^{CA3}	1000	–	Number of excitatory neurons in CA3 hippocampal network
N_i^{CA3}	100	–	Number of inhibitory neurons in CA3 hippocampal network
N_e^{CA1}	1000	–	Number of excitatory neurons in CA1 hippocampal network
N_i^{CA1}	100	–	Number of inhibitory neurons in CA1 hippocampal network
N_e^{CX1}	8000	–	Number of excitatory neurons in CX1
N_i^{CX1}	2000	–	Number of inhibitory neurons in CX1
N_e^{CX2}	8000	–	Number of excitatory neurons in CX2
N_i^{CX2}	2000	–	Number of inhibitory neurons in CX2

Acknowledgments

This project was supported by the National Natural Science Foundation of China (Grant Nos. 12272002 and 12372061), the R&D Program of Beijing Municipal Education Commission (Grant No. KM202310009004), the North China University of Technology (Grant No. 2023XN075-01), and the Youth Research Special Project of the North China University of Technology (Grant No. 2025NCUTYRSP051).

References

[1] Guskjolen A and Cembrowski M S 2023 *Mol. Psychiatry* **28** 3207
[2] Kandel E R, Dudai Y and Mayford M R 2014 *Cell* **157** 163
[3] Knowlton B J and Fanselow M S 1998 *Curr. Opin. Neurobiol.* **8** 293
[4] Marshall L and Born J 2007 *Trends Cogn. Sci.* **11** 442
[5] Aggleton J P and O'Mara S M 2022 *Nat. Rev. Neurosci.* **23** 505
[6] Lamprecht R and LeDoux J 2004 *Nat. Rev. Neurosci.* **5** 45
[7] Buckner R L, Kelley W M and Petersen S E 1999 *Nat. Neurosci.* **2** 311
[8] Sommer M A 2003 *Curr. Opin. Neurobiol.* **13** 663
[9] Bragin A, Engel J Jr, Wilson C L, Fried I and Mathern G W 1999 *Epilepsia* **40** 127
[10] Lu N, Xing D Q, Sheng T and Lu W 2017 *Acta Physiol. Sinica* **69** 647
[11] Roumis D K and Frank L M 2015 *Curr. Opin. Neurobiol.* **35** 6
[12] Yang Y C, Li Y Z and Sun X J 2025 *Nonlinear Dyn.* **113** 799
[13] Buzsaki G 2015 *Hippocampus* **25** 1073
[14] Nokia M S and Penttonen M 2022 *Front. Neural Circuits* **16** 885684
[15] Pfeiffer B E and Foster D J 2013 *Nature* **497** 74
[16] Sadowski J H L P, Jones M W and Mellor J R 2016 *Cell Rep.* **14** 1916
[17] Yonelinas A P, Ranganath C, Ekstrom A D and Wiltgen B J 2019 *Nat. Rev. Neurosci.* **20** 364
[18] Roux L, Hu B, Eichler R, Stark E and Buzsaki G 2017 *Nat. Neurosci.* **20** 845
[19] Si Y Y, Zhang H H and Shen Z 2025 *Int. J. Bifurcat. Chaos* **35** 2550060
[20] Goutagny R, Gu N, Cavanagh C, Jackson J, Chabot J G, Quirion R, Krantic S and Williams S 2013 *Eur. J. Neurosci.* **37** 1896
[21] Steriade M and Amzica F 2003 *Epilepsia* **44** 9
[22] Marshall L, Helgadottir H, Molle M and Born J 2006 *Nature* **444** 610
[23] Tsai Y T, Chan H L, Lee S T, Tu P H, Chang B L and Wu T 2010 *Neurosci. Lett.* **485** 173
[24] Boutin A, Pinsard B, Bore A, Carrier J, Fogel S M and Doyon J 2018 *Neuroimage* **169** 419
[25] Eschenko O, Molle M, Born J and Sara S J 2006 *J. Neurosci.* **26** 12914
[26] Ghorbani M, Mehta M, Bruinsma R and Levine A J 2012 *Phys. Rev. E* **85** 021908
[27] Gonzalez J, Cavelli M, Mondino A, Castro-Zaballa S, Brankack J, Draguhn A, Torterolo P and Tort A B L 2023 *Pflugers Arch.* **475** 49
[28] Foroutannia A, Ghasemi M, Parastesh F, Jafari S and Perc M 2020 *Nonlinear Dyn.* **100** 2699
[29] Foroutannia A, Nazarimehr F, Ghasemi M and Jafari S 2021 *J. Theor. Biol.* **528** 110837
[30] Lafon B, Henin S, Huang Y, Friedman D, Melloni L, Thesen T, Doyle W, Buzsaki G, Devinsky O and Parra L C 2017 *Nat. Commun.* **8** 1199
[31] Yang L, Zhang H H, Sun Z K, Du L and Chen G R 2024 *Nonlinear Dyn.* **112** 7499
[32] Azimi A, Alizadeh Z and Ghorbani M 2021 *Neuroimage* **243** 118485
[33] Girardeau G, Benchenane K, Wiener S I, Buzsaki G and Zugaro M B 2009 *Nat. Neurosci.* **12** 1222
[34] Colgin L L 2016 *Nat. Rev. Neurosci.* **17** 239
[35] Jia Y B, Gu H G and Wang X J 2025 *Chaos* **35**
[36] Jefferys J G R, de la Prida L M, Wendling F, Bragin A, Avoli M, Timofeev I and da Silva F H L 2012 *Prog. Neurobiol.* **98** 250
[37] Wang Z H, Ge Y T and Duan L X 2025 *Chaos Solitons Fractals* **196** 116322
[38] Wang Z H, Wei X D and Duan L X 2025 *Cogn. Neurodyn.* **19** 37
[39] Yuan Y, Chen Y D and Li X L 2016 *Chin. Phys. B* **25** 084301
[40] Leminen M M, Virkkala J, Saure E, *et al.* 2017 *Sleep* **40** zsx003
[41] Geva-Sagiv M, Mankin E A, Eliashiv D, Epstein S, Cherry N, Kalender G, Tchemodanov N, Nir Y and Fried I 2023 *Nat. Neurosci.* **26** 1100
[42] Ladenbauer J, Ladenbauer J, Kulzow N, de Boor R, Avramova E, Grittner U and Floel A 2017 *J. Neurosci.* **37** 7111
[43] Yin L N, Han F and Wang Q Y 2024 *Cogn. Neurodyn.* **18** 1895
[44] Fan D G, Chen J, Hou S G, Song Z Y, Baier G and Wang Q Y 2025 *Chaos Solitons Fractals* **191** 115754